Mapping Nanostructure: A Systematic Enumeration of Nanomaterials by Assembling Nanobuilding Blocks at Crystallographic Positions

Dean C. Sayle,[†,*] Sudipta Seal,[‡,§] Zhongwu Wang,[⊥] Benoît C. Mangili,[†] David W. Price,[∥] Ajay S. Karakoti,[‡,#] Satyanarayana V. T. N. Kuchibhatla,[‡,#] Quan Hao,[⊥] Günter Möbus,[¶] Xiaojing Xu,[¶] and Thi X. T. Sayle[†]

[†]Department of Applied Science, Security and Resilience Defence College of Management and Technology, Cranfield University, Defence Academy of the United Kingdom, Shrivenham SN6 8LA, U.K., [‡]Surface Engineering and Nanotechnology Facility, Advanced Materials Processing and Analysis Center, Department of Mechanical Materials and Aerospace Engineering, University of Central Florida, Orlando, Florida 32862, [§]Nanoscience and Technology Center, University of Central Florida, Orlando, Florida 32862, [⊥]Cornell High Energy Synchrotron Source, Wilson Laboratory, Cornell University, New York 14853, [∥]Material Science Research Division, Research and Applied Science, AWE, Aldermaston RG7 4PR, U.K., [#]Pacific Northwest National Laboratory, 3335 Q Avenue, Richland, Washington 99352, and [¶]Department of Engineering Materials, University of Sheffield, Mappin Street, Sheffield S1 3JD, U.K.

ABSTRACT Nanomaterials synthesized from nanobuilding blocks promise size-dependent properties, associated with individual nanoparticles, together with collective properties of ordered arrays. However, one cannot position nanoparticles at specific locations; rather innovative ways of coaxing these particles to self-assemble must be devised. Conversely, *model* nanoparticles can be placed in any desired position, which enables a systematic enumeration of nanostructure from model nanobuilding blocks. This is desirable because a list of chemically feasible hypothetical structures will help guide the design of strategies leading to their synthesis. Moreover, the models can help characterize nanostructure, calculate (predict) properties, or simulate processes. Here, we start to formulate and use a simulation strategy to generate atomistic models of nanomaterials, which can, potentially, be synthesized from nanobuilding block precursors. Clearly, this represents a formidable task because the number of ways nanoparticles can be arranged into a superlattice is infinite. Nevertheless, numerical tools are available to help build nanoparticle arrays in a systematic way. Here, we exploit the "rules of crystallography" and position nanoparticles, rather than atoms, at crystallographic sites. Specifically, we explore nanoparticle arrays with cubic, tetragonal, and hexagonal symmetries together with primitive, face centered cubic and body centered cubic nanoparticle "packing". We also explore binary nanoparticle superlattices. The resulting nanomaterials, spanning CeO_2, Ti-doped CeO_2, ZnO, ZnS, MgO, CaO, SrO, and BaO, comprise framework architectures, with cavities interconnected by channels traversing (zero), one, two and three dimensions. The final, fully atomistic models comprise three hierarchical levels of structural complexity: crystal structure, microstructure (*i.e.*, grain boundaries, dislocations), and superlattice structure.

KEYWORDS: molecular dynamics · nanobuilding blocks · crystallography · mesostructure · oxide · atomistic model · nanostructure · X-ray diffraction · electron microscopy

Nanomaterials, derived from nanobuilding blocks, display a wealth of novel properties that combine the unique size-tuned properties of a single nanocrystal with the striking collective properties of newly created ordered arrays[1–4] and boast applications spanning computer chips, catalysis, fuel cells, sensors, battery and energy storage devices, and corrosion.[5] It is unlikely that any application or device will utilize a single nanoparticle; rather, to exploit the size-dependent properties of nanoparticles requires their (self) assembly into superlattices.[6,7]

Previously, we used simulated amorphization and crystallization to generate models of the nanobuilding blocks. For example, Figure 1 shows model structures of CeO_2[8] and Ti-doped CeO_2 nanocrystals[9] together with high-resolution transmission electron micrographs (HRTEM) and a tomogramme revealing quantitative agreement between experiment and theory. In particular, when doped with titanium, an amorphous TiO_2 shell encapsulates the inner CeO_2 core, resulting in a morphological transformation from truncated octahedral to spherical.

These nanoparticles can be used as building blocks for the nanomaterials.[10] However, it is not clear how nanobuilding blocks pack to form superlattices. For example, if nanobuilding blocks have the ability to pack in a similar way to atoms, then one can envisage the number of nanomaterials reflecting the number of crystal structures (notwithstanding relative sizes and or nanobuilding block rotations *etc.*).

Ultimately, one desires the ability to position one-, two-, and three-dimensional arrays of nanoparticles at (any) specified location with precision. Indeed, the drive to devise synthetic solutions to this problem is as intense as that given to the synthesis of the nanobuilding blocks.[11] However, experiment is faced with a daunting chal-

*Address correspondence to d.c.sayle@cranfield.ac.uk.

Received for review February 1, 2008 and accepted May 27, 2008.

Published online June 24, 2008.
10.1021/nn800065g CCC: $40.75

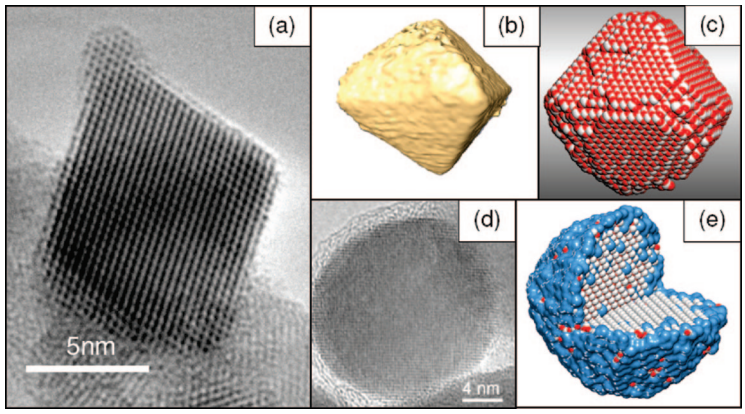

Figure 1. Nanobuilding blocks. (a) HRTEM of a CeO_2 nanocrystal; (b) three-dimensional tomogramme of a CeO_2 nanocrystal generated from computer-aided tomography of sequentially oriented TEM images; (c) atomistic model of a CeO_2 nanocrystal; (d) Ti-doped CeO_2 nanocrystal showing the (amorphous) TiO_2 shell encapsulating the inner (crystalline) CeO_2 core rendering it spherical; (e) atomistic model of a Ti-doped CeO_2 nanocrystal.

lenge: One cannot position nanoparticles at specific locations; rather innovative ways of coaxing these particles to self-assemble must be devised, such as using surfactants or by exploiting the charge or dipole associated with the nanoparticles.[12–14] Conversely, it is possible for the theoretician to generate an atomistic model comprising a periodic array of nanoparticles located at *any* chosen positions. This facilitates the opportunity to systematically enumerate nanostructure from nanobuilding blocks.

In this study, we predict the atomistic structure of a variety of chemically feasible hypothetical nanostructures, which will be valuable because the model structures will help facilitate the design of strategies leading to their synthesis.[15] In addition, the atomistic models can be used to calculate particular properties and/or simulate important processes. Specifically, they can be used to identify nanomaterials with optimized, exceptional, or perhaps new properties, while screening those which are predicted to have ordinary or, conversely, undesirable properties.

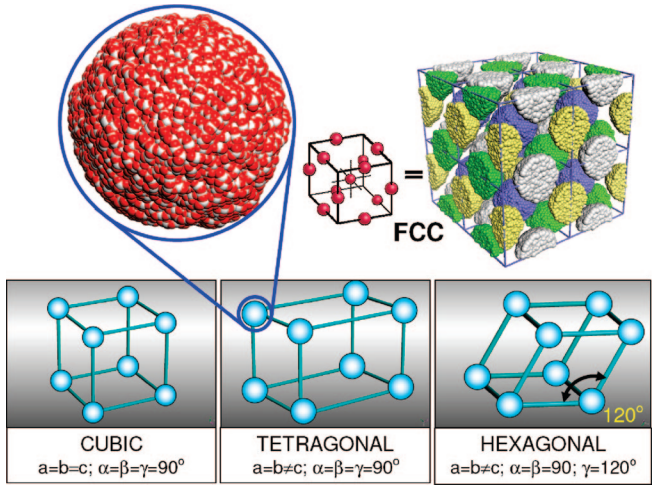

Figure 2. Schematic illustrating the positioning of nanobuilding blocks into periodic crystallographic arrays. Top left, shows a spherical nanobuilding block, top right a superlattice comprising nanobuilding blocks located at face centred cubic (FCC) lattice points.

One can envisage a wealth of (numerical) tools that can be used to explore nanostructure in a systematic way. For example, Friedrichs and coworkers used a strategy based on tiling theory to enumerate crystal networks.[16] Here, we develop and start to use a simulation strategy, based upon the "rules of crystallography" to help map nanostructure. We note that our approach (in its present form) will not prove *exhaustive* in enumerating nanostructure. Neither will it be definitive in unravelling the nanostructure landscape. For example, some nanomaterials, such as multiwalled tubes, have no translational symmetry,[17,18] which is a complexity in the nanomaterial landscape that one might not have anticipated. Rather, our method will enable a systematic exploration of hypothetical nanostructures and help us to probe the nanostructure landscape. Here, we have chosen to use crystallography, which has developed over the past 100 years, to provide a robust, rigorous, systematic, and validated platform to help map nanostructure.[19] Specifically, we position nanobuilding blocks, rather than atoms, at crystallographic positions (Figure 2). We test and use the strategy to explore a broad range of nanostructures by considering:

- Three different crystal systems: cubic, hexagonal, and tetragonal together with primitive centered, body centered, or face centered (Bravais lattice)
- Various sizes, shapes, and types of nanobuilding blocks including binary superlattices.[20]
- A variety of materials and crystal structures including: CeO_2, Ti-doped CeO_2, ZnO, ZnS, MgO, CaO, SrO, and BaO

We also need to ensure that the nanostructures are chemically feasible, and therefore, the model nanostructures must reflect a real nanomaterial on all the length scales (up to nanometers) that we consider. Specifically, our models must crystallize into (i) the correct crystal structure; (ii) the microstructural features that one expects in a real nanomaterial must also be incorporated into the model. This may include, for example, dislocations and grain boundaries, point defects (vacancies, interstitials), surfaces exposed and (internal) morphology, lattice strain and surface relaxation, and (iii) the particular architecture associated with the nanostructure must be accommodated by the model, such as zero-, one-, two-, and three-dimensional channels similar to those observed experimentally. However, perhaps most important, the models must be useful in a way benefiting experiment. Specifically the atomistic models generated will be valuable because they will help (experiment) characterize nanostructure. In particular, the atomistic structure deep within the porous structure is a region notoriously difficult to explore experimentally. The resulting models, similar to the field

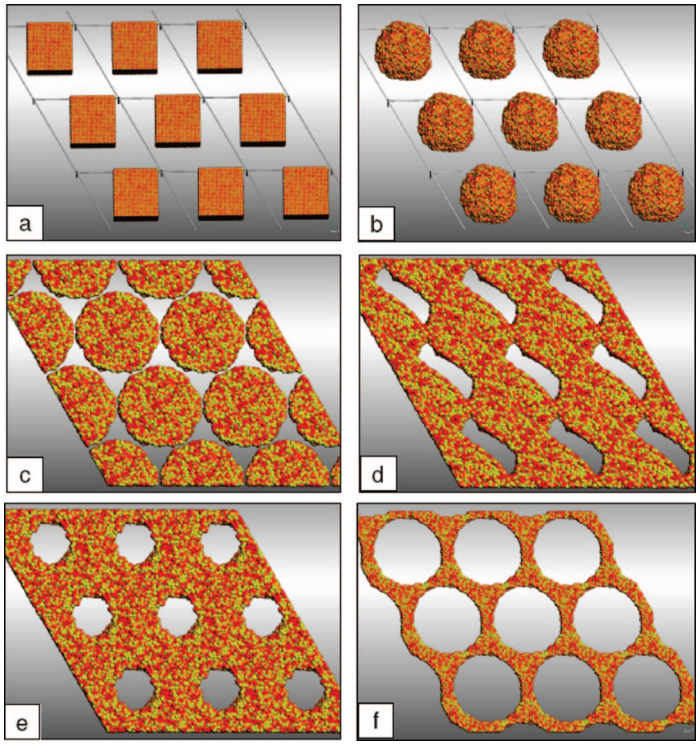

Figure 3. Evolution of framework architecture *via* nanoparticle assembly. (a) Starting structure comprising 25 200 atom MgO nanoparticles assembled into a hexagonal array; (b) molten/amorphous nanoparticles; (c) nanoparticles start to aggregate; (d) channels starting to evolve *via* necking of neighboring nanoparticles; (e) small channels with thick walls; and (f) larger channels with thin walls. Oxygen is red and magnesium is yellow.

of zeolite modeling and simulation, can be used to calculate important properties, including, for example, surface vacancy formation energies (applications include catalysis, sensor), segregation, and mechanical properties. The models can also be used to simulate pertinent processes including gas and/or liquid flow, ionic transport, confinement (one-, two-, and three-dimensional).

Nanomaterials exhibit structural complexity, which is difficult to represent adequately within an atomistic model. In particular, the model needs to be sufficiently realistic in that it can be used to calculate properties and simulate processes with sufficient accuracy such that the models and results derived from using the models are of value to experiment. Structural features, pertaining to the (real) nanomaterial, evolve as a consequence of the synthetic pathways used in its fabrication, and therefore, if we are able to simulate these synthetic pathways, then we will be able to capture the important structural detail.

Atomistic simulation has not matured sufficiently to *directly* simulate synthesis fully; neither are computational facilities available to perform such simulations if it were thus advanced. Rather, this study focuses primarily in predicting nanostructure systematically and, in future, building upon this preliminary study to correlate nanostructure with properties to provide experiment with valuable insight. Accordingly, approximations pertaining to "simulating synthesis" must be introduced to facilitate tenable simulations and thus enable progress to be made in this area. To this end, we subdivide synthesis into two major components and use key representative experimental studies to help direct our simulations:

Nanoparticle Self-Assembly. This experimental approach, which facilitates porous structures including networks of cavities and interconnecting channels, is typified experimentally by Deshpande and co-workers, who self-assembled crystalline ceria nanoparticles into framework architectures[21] and Kuchibhatla and co-workers who assembled ceria nanocrystals into octahedral superlattices;[22] a wealth of similar approaches are reviewed.[4] Thus after the nanoparticles have been positioned into crystallographic sites, we then allow them to self-assemble into a nanostructure.

Crystallization. Crystallization, which facilitates evolution of the crystal structure together with microstructural features (including, for example, grain boundaries, dislocations, point defects, internal morphology, lattice strain), is exemplified by Lu *et al*. who crystallized amorphous Nb−Ta and Mg−Ta mixed oxides, in a vacuum, into highly ordered 2D hexagonal structures.[23] The resulting framework structures were polycrystalline, yet retained the 2D array of channels of the amorphous precursors.

In this present study, we direct our simulations to mimic such experiments. In particular, we position nanobuilding blocks into crystallographic arrays and then simulate their self-assembly into nanomaterials. We also simulate directly the crystallization of the material starting from amorphous precursors.

Generation of Nanomaterials from Nanobuilding Units. We first describe the simulations pertaining to generating nanostructures derived from amorphous nanobuilding blocks and then describe the generation of nanostructures from crystalline nanobuilding blocks.

Amorphous Nanobuilding Blocks. A hexagonal array of (cuboidal) MgO nanoparticles (Figure 3), each comprising about 25 000 atoms (Figure 3a), were amorphized/melted by performing MD simulation at temperatures above the melting point, which resulted in spherical nanoparticles (Figure 3b). The nanoparticles then aggregated with their periodic neighbors (Figure 3c,d), facilitating the evolution of a two-dimensional hexagonal array of cylindrical channels (Figure 3e). The size of the channels and/or thickness of the channel walls was controlled by applying tension (larger channels) or

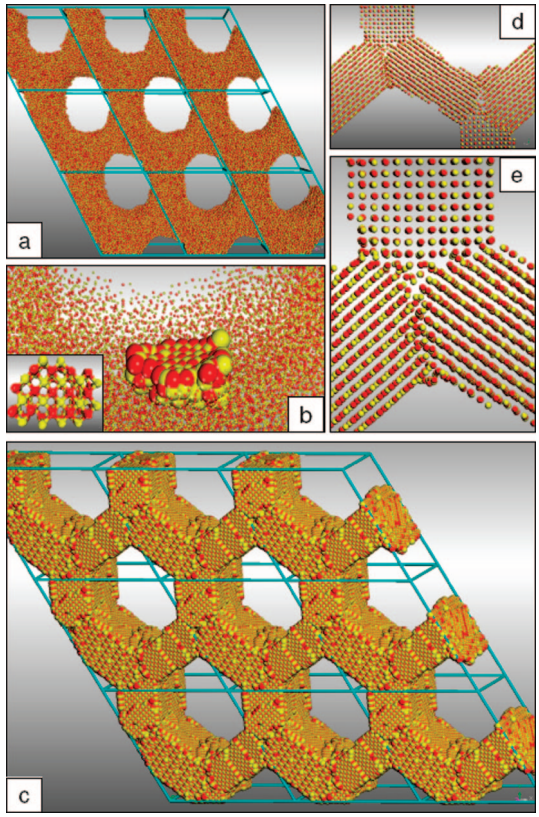

Figure 4. Crystallization of (amorphous) framework architecture: (a) starting structure; (b) structure of a crystalline (nucleating) seed that spontaneously evolves at the surface of one of the channels enveloped by an amorphous sea of ions; inset shows the (rocksalt) structure of the crystalline seed more clearly; (c) final crystalline structure; (d) enlarged segment of (c) revealing the structure of the grain boundaries; (e) enlarged version of (d). Oxygen is red and magnesium is yellow.

compression (smaller channels) (Figure 3e,f), which reflects the presence of surfactant or colloidal "scaffold".[11]

The amorphous framework was then crystallized by applying MD simulation at reduced temperatures. Specifically, a 2D array of hexagonal channels, 6 nm in diameter and 3 nm wall thickness (Figure 3e), was crystallized: Under MD simulation, performed at 2000 K, a nucleating seed spontaneously evolves on the surface of one of the channels and expresses the (energetically most stable) MgO(100) surface; the embryonic structure of this seed is shown in Figure 4b. As crystallization continues, molten ions condense onto the surface of this nucleating seed, propagating crystallization, and consuming eventually all the amorphous ions. The final structure is shown in Figure 4c−e.

Experimentally, mesoporous MgO, with crystalline walls, was synthesized by Roggenbuck and Tiemann.[24,25] A TEM image of the mesoporous MgO is shown in Figure 5a and has a cell constant (corresponding to the hexagonal pore arrangement) of 10 nm, a pore diameter of 7 nm, and a wall thickness of 3 nm. Our model structure, similar to experiment, comprises a hexagonal array of channels with pore diameters of 7 nm, a wall thickness of 2.8 nm, and a surface area calculated to be about 30 m^2/g.

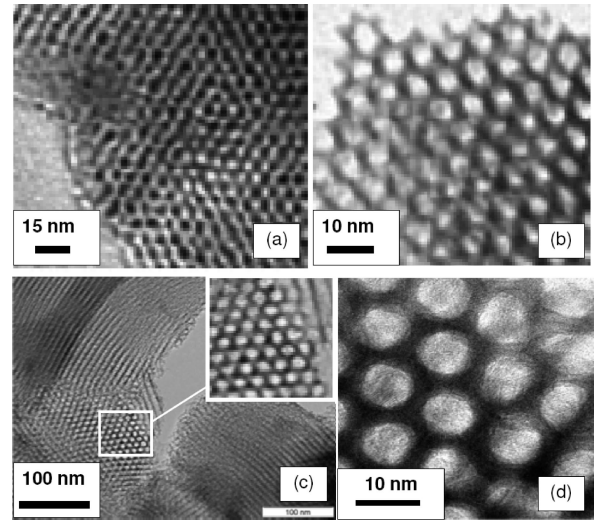

Figure 5. HRTEM of mesoporous oxides: (a) MgO,[24] (b) Mg−Ta mixed oxide,[23] (c) SiO_2; (d) TiO_2.[26]

Analogous simulation strategies were used to generate models for CeO_2 (3000 K), Ti−CeO_2 (3000 K), ZnS (1500 K), ZnO (1500 K), CaO (2000 K), SrO (2000 K), and BaO (1600 K); the figures in parentheses correspond to the temperatures required to facilitate successful crystallizations of the framework architectures. We simulated primitive (P), body centred cubic (BCC), and close packed (FCC, HCP) filling of the simulation cells.

Crystalline Nanobuilding Blocks. Nanostructures were also generated using *precrystallized* nanobuilding blocks. In particular, crystalline CeO_2 and 25% Ti-doped CeO_2 nanobuilding blocks that we generated previously[9] were placed into a cubic cell with primitive (Ti−CeO_2) and FCC (CeO_2) packing. The constant pressure MD simulation was applied at 3000 K under 1 GPa pressure for Ti−CeO_2 (Figure 6) and 3400 K at zero pressure for CeO_2. We note that, for the latter, no pressure was required because the internanocrystal attraction was sufficiently strong to agglomerate the nanobuilding blocks within the (limited—typically nanosecond) time scale accessible to the MD simulations.

RESULTS

Here, we categorize the model structures as a function of the crystal structure, into which the atoms crystallize, and the super lattice—specifically, the symmetry of the cell and the packing of the nanobuilding blocks within this cell.

Cubic Crystal Structure/Hexagonal Superlattice (P). Amorphous nanobuilding blocks of MgO, CaO, SrO, and BaO were positioned, with primitive (P) packing, into hexagonal supercells and simulated, under MD, using the procedures described above and in Supporting Information, S1. Graphical images of the atom positions comprising MgO, CaO, SrO, and BaO nanostructures are shown in Figure 7a−d, respectively. Inspection of

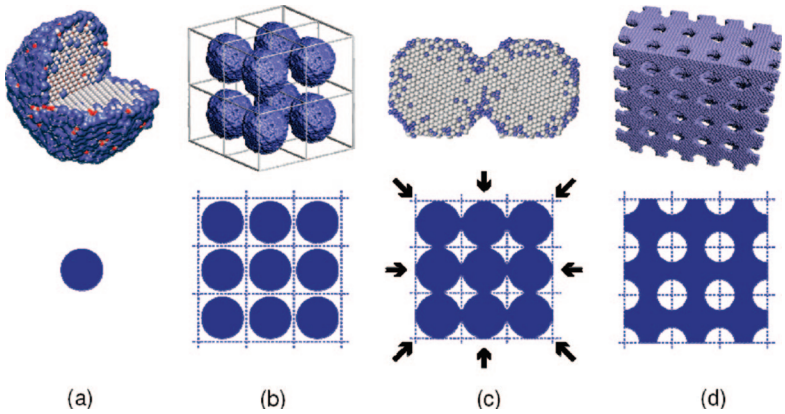

Figure 6. Ti−CeO_2 superlattice generated from spherical Ti-doped nanobuilding blocks. (a) Ti−CeO_2 nanobuilding block, (b) Ti−CeO_2 nanobuilding blocks positioned at (cubic) lattice positions. (c) Under MD simulation, the nanoparticles attract one another, move closer together, and agglomerate, facilitating channels in three perpendicular directions. (d) Final structure. Top images are full atomistic models, and bottom figures are schematics illustrating the process.

the models reveals that the framework architectures comprise hexagonal arrays of channels, which traverse through the structure in one dimension. Further analysis, using graphical techniques, reveals that the oxides crystallize into the rocksalt structure and expose {100}, which are, thermodynamically, the most stable surfaces. It is important to understand and characterize the surface structure because it is central to the chemistry that can occur at the internal surfaces. Accordingly, the radial distribution function, calculated for Ba−O, is shown in Figure 7e and reveals peak broadening; the nearest neighbor Ba−O distances span 2.3−3.1 Å with an average of 2.75 Å. This indicates that there is significant ionic relaxation within the framework, which will be reflected in changes to the physical, chemical, and mechanical properties of these structures compared with the parent, bulk materials.

The rocksalt (cubic) crystal structure is not commensurate with the (hexagonal) symmetry of the array of channels, neither is it commensurate with the hexagonal profile of the channel and therefore one might question the exposure of {100} surfaces. However, closer inspection, using graphical techniques, reveals (triple) grain boundaries (Figure 4d,e), which facilitate both the hexagonal profile of the channels and channel arrays. We also predict that, as the wall thickness reduces, the strain associated with the curvature of the channel cannot be sustained; rather a polycrystalline structure evolves (Figure 7a,b). The strain within the lattice can also be extracted from the models by calculating, for example, "local" bond distances following refs 27 and 28 and calculated radial distribution function (Figure 7e). Clearly, it is difficult to characterize the internal surface structures using TEM (such as those presented in Figure 5), and therefore, the simulated models provide valuable insights and prediction.

Cubic Crystal Structure/Tetragonal Superlattice (P). Here, amorphous MgO, CaO, SrO, and BaO nanobuilding blocks were positioned into a tetragonal supercell and simulated, using MD into nanostructures. The dimensions of the supercells were adjusted to facilitate framework architectures comprising cavities interconnected by channels traversing three perpendicular directions.[45] The atom positions comprising the unit cell of CaO are shown in Figure 8a, which reveals a cavity interconnected by perpendicular channels. The surface structure is shown without atoms (surface rendered model) in Figure 8b and reveals, more clearly, that the curvature of the cavity and interconnecting channels is facilitated by predominant exposure of {100} together with a high concentration of surface steps. The diameter of the cavity is about 9 nm. Similarly, inspection of MgO and SrO (Figure 8c,d) reveals predominant exposure of {100} together with a high

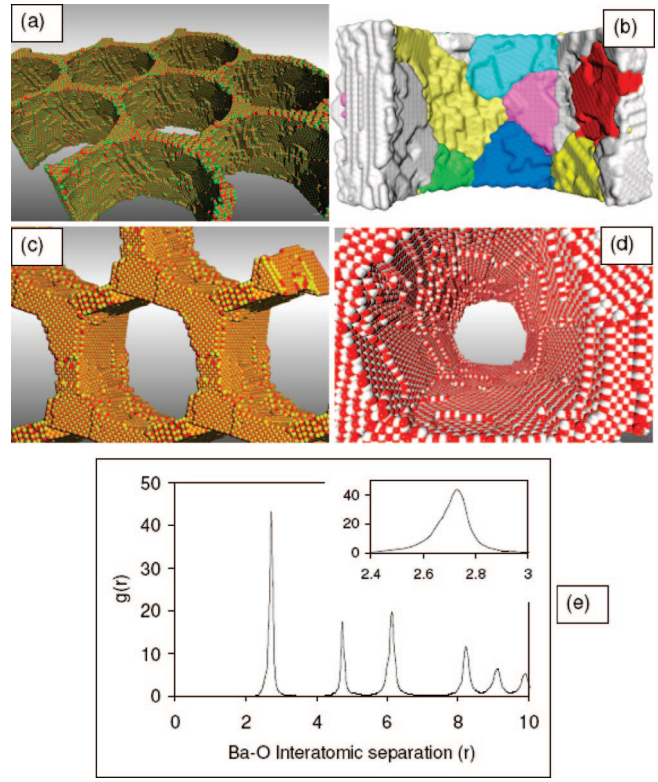

Figure 7. Atomistic models of mesoporous rocksalt-structured oxides generated by positioning the oxide nanobuilding blocks into a hexagonal cell. (a) MgO; (b) CaO; (c) SrO, (d) BaO. In (a), (c), and (d), the atom positions are represented by spheres, and in (b), a surface rendered model is shown; the various misoriented grains are represented by different colors. Mg is colored green, Sr is yellow, Ba is white, and O is red. (e) Calculated Ba−O radial distribution function. Inset shows the nearest neighbor peak enlarged; interatomic separations are given in angstroms.

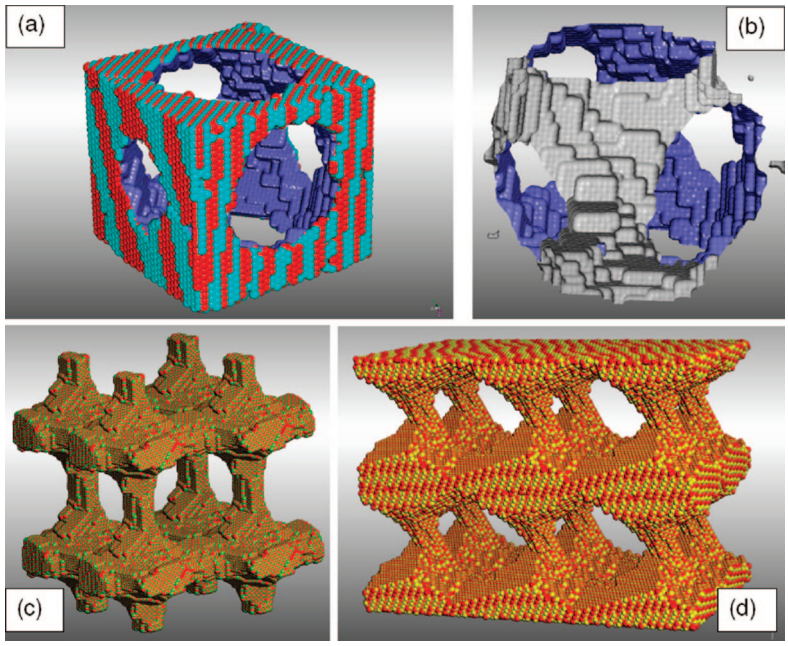

Figure 8. Atomistic models of mesoporous rocksalt-structured oxides generated by positioning the oxide nanobuilding blocks into a tetragonal cell. (a) CaO sphere model representation of the atom positions; (b) CaO, surface rendered, showing more clearly the size and shape of the cavities within the CaO; (c) MgO, sphere model, (d) SrO sphere model. Ca is colored blue, Mg is green, Sr is yellow, and O is red.

concentration of steps and edges, which facilitate the (concave and convex) curvatures of the internal surfaces and thus the complex, porous architectures. We predict, based upon the model structures, that the chemistries associated with these materials will likely reflect chemistries associated with MO(100) (plateau), MO(110) (steps), and MO(111) (corners); M = metal. We note that MO(111) surfaces are dipolar[29] and can facet into MO(100) and MO(110)—plateau and steps with corner sites. A high concentration of low coordinated corner sites and hence labile surface species is indicative of high reactivity; the coordination number of rocksalt structured oxides change from six in the parent bulk material to three (corner site).

Theoretically, porous materials comprising cavities with cubic morphologies, interconnected by three-dimensional perpendicular channels with square profile and exposing wholly MO{100}, can be cut from rocksalt-structured materials. It is likely that these structures are thermodynamically stable compared with the structures presented above because (energetically deleterious) grain boundaries or channel curvatures are not required to facilitate such architectures. These structures could potentially be synthesized using precrystallized rocksalt-structured nano(cube)building blocks.[30] However, in this study, we have generated the models using a mimetic approach where nanostructure synthesis involves crystallization from amorphous precursors,[23] which will necessarily have curved (minimal surface[45]) starting configurations. The consequence of this is that the high concentration of surface steps needed to facilitate the curvatures of the channels and cavities will facilitate low coordinated surface atoms and therefore be inextricably linked to the surface chemistry. Moreover, such structures will likely present different reactivities compared with the parent bulk material.

Hexagonal Crystal Structure/Hexagonal Superlattice (P). Amorphous nanobuilding blocks of ZnS and ZnO, each comprising 25,200 atoms, were placed, with primitive filling, into a hexagonal supercell. The nanoparticles were then aggregated into a mesoporous framework, following the simulation strategy described above, and crystallized at 1700K. The final, crystallized framework structures are presented in Figure 9a−c and d−f for ZnO and ZnS, respectively. The ZnO structure comprises a hexagonal array of channels with hexagonal profile. This structure might have been anticipated because these structures can be "cut" from the (single crystal) parent material. However, inspection of the hexagonal channel profile (Figure 9b) reveals that the framework ZnO is not a single crystal; rather it comprises several misoriented grains. Moreover, Figure 9c confirms that the hexagonal profile is facilitated not by the (hexagonal) crystal structure but by grain boundaries. On the other hand, 120° angles required to facilitate a hexagonal channel were observed in some of the ZnO model structures; an enlarged segment of such a channel showing the crystal structure is shown in Figure 9d. We attribute the polycrystalline framework and associated grain boundaries (which will impact deleteriously upon the thermodynamic stability) to kinetic factors. In particular, similar to the behavior described in Figure 4a, a crystalline seed spontaneously evolves at the surface. The seed reaches a nucleating size and propagates crystallization of the surrounding framework lattice. However, before this seed facilitates crystallization of the entire framework, another seed evolves on a different surface. The probability that the orientations of the two crystalline seeds are commensurate (to facilitate a single crystal) is low, and therefore, as the crystallization fronts, emanating from each seed, impinge upon one another a grain boundary is formed. We note that the grain boundaries are curved (both Figure 4e and Figure 9c), which offers further support that the boundary is formed from two crystallizing fronts impinging upon one another. Further evidence is provided in Figure 9e,f, which reveals a polycrystalline ZnS framework; a small segment of this structure (inset) was cut to reveal that the ZnS had crystallized into the wurtzite structure. We note that "simulated annealing" (high-temperature MD simulation performed in excess of the time required for full crystallization—1700 K for several nanoseconds), revealed sintering of the smaller crystalline grains into a larger grain.[31] We hypothesize that this Oswald ripening will be influ-

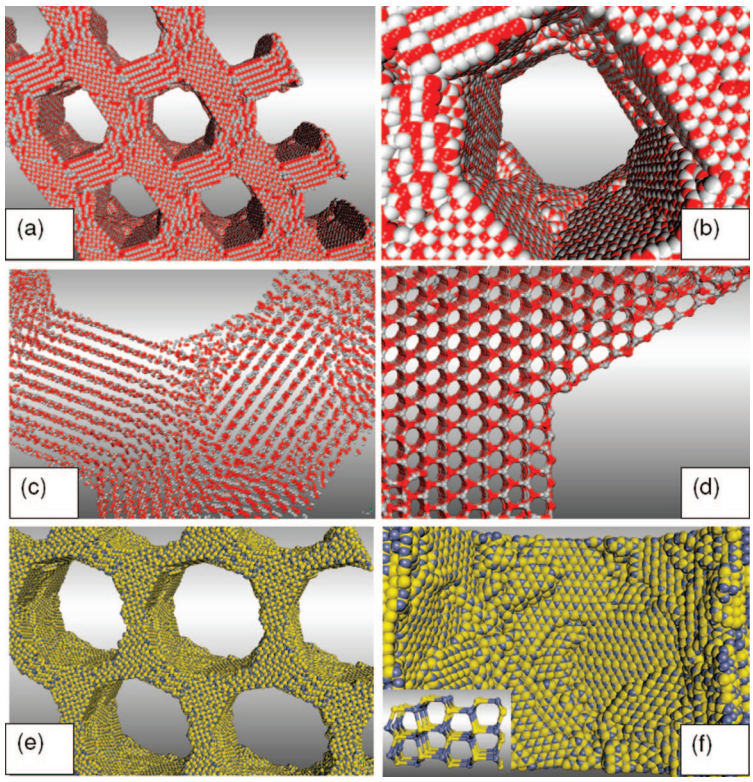

Figure 9. Atomistic models of mesoporous ZnO (a−d) and ZnS (e, f), which were generated by positioning ZnO and ZnS nanobuilding blocks into hexagonal cells with primitive packing. (a) View looking along the hexagonal array of channels in ZnO. (b) Enlarged view of (a). (c) Enlarged segment of the ZnO framework where the atom positions are represented by small spheres to reveal that the hexagonal profiles of the channels are facilitated by misoriented grains. The curved structure of the triple junction is also evident from the figure. (d) Here, in contrast to (c), the 120° angle of the hexagonal channel is facilitated by the crystal structure of the ZnO and the figure shows a single crystal. (e) View looking along the hexagonal array of channels in ZnS. The channel cross section appears more octagonal than hexagonal. (f) View looking at a cross section of one of the channels showing a wealth of steps and edges. Part of the framework structure is shown (inset) revealing that the ZnS crystallizes into the wurtzite structure. We note that the framework is polycrystalline and comprises many misoriented grains. Zn is colored white (ZnO) and blue (ZnS), O is red, and S is yellow.

enced by the framework architecture and propose to test this with further simulations.

Thus far we have considered only primitive packing of the simulation cell with nanobuilding blocks. On the other hand, a superlattice comprising *close-packed* nanobuilding blocks is perhaps more likely, and therefore we now consider these structures.

Cubic Crystal Structure/Cubic Superlattice (FCC). Here, amorphous MgO nanobuilding blocks, each comprising 25 200 atoms, were positioned at face centered cubic FCC lattice points within a simulation cell (Figure 2). The (infinitely repeating) unit cell comprised four MgO nanobuilding block (100 800 atoms). Under MD, performed at 4000 K, the nanoparticles agglomerated, facilitating a complex morphology with minimal surface.[32] The system was then crystallized by performing MD at 2000 K and cooled to 10 K. The structure of the amorphous and crystallized system is shown in Figure 10. The structural complexity of these porous structures is difficult to rationalize and do not appear, at first inspection, similar to the starting configuration (FCC packing of a cubic cell with amorphous spherical nanobuilding blocks, Figure 2). Here, extensive use of molecular graphics was used to characterize these complex model structures. In particular, similar to rationalizing a crystal structure using Miller indices, we can rationalize the nanostructure by annotating low index planes corresponding to the *superlattice*. Accordingly, we present the (FCC) model structure, oriented along [111], [110], and [100], in Figure 10a−c, respectively. One can observe and rationalize more readily from these structures the complex structure of interconnecting cavities and channels. For example, if one inspects Figure 10a, one can identify {111} (three yellow arrows in the figure), which correspond to the superlattice. The same can be performed for Figure 10b,c, although {110} presents more of a visual challenge.

After crystallization, the low temperature structure (Figure 10d) retains the framework architecture of the original amorphous starting structure. Close inspection of the surface structure reveals that the (rocksalt) crystal structure exposes predominantly {100} surfaces, the high curvature of the channels and cavities facilitated by the polycrystalline nature of the MgO, similar to the structure shown in Figure 7a together with the presence of a high concentration of surface steps and edges.

Hexagonal Crystal Structure/Cubic Superlattice (FCC). In Figure 11a, mesoporous ZnO (HRTEM image) is shown,[33] which was synthesized by assembling polystyrene latex spheres on a substrate and then infiltrating with ZnO by galvanostatic cathodic deposition. The system was then heated to 600 °C to remove the polystyrene template. Field emission scanning electron microscopy revealed a well-formed, regular 3D periodic porous structure comprising spherical holes arranged in a face centered cubic (FCC) structure. The "chemistry" (reactivity) of this system is likely dependent upon the internal morphology and surfaces exposed. The structure has similar characteristics to our simulated model, and therefore, we propose that simulation can be used to generate atomistic models for these structures and help

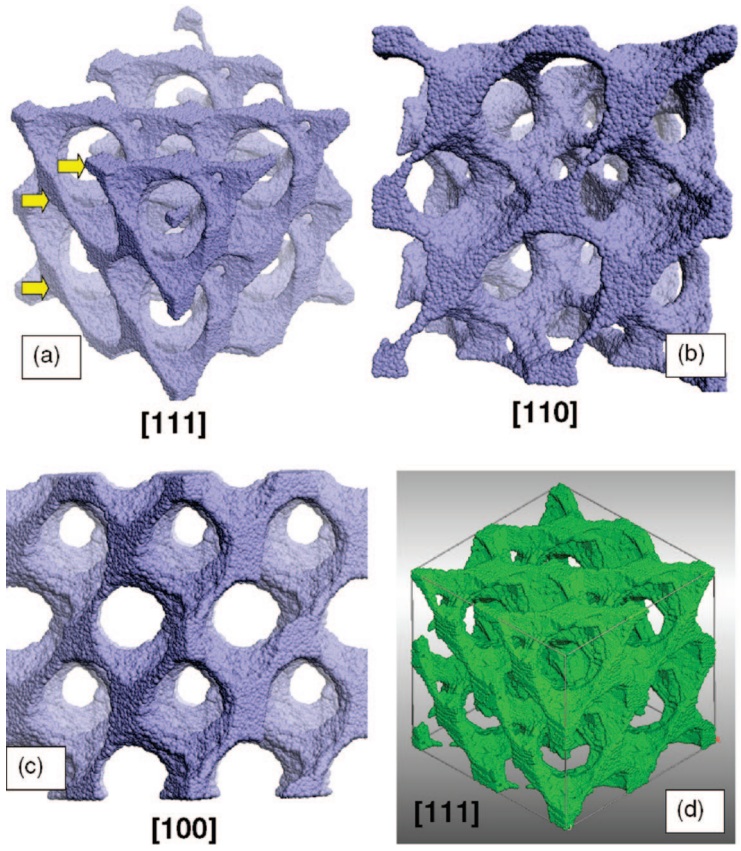

Figure 10. Atomistic models of mesoporous MgO generated by positioning a close packed (FCC) array of MgO nanobuilding blocks into a cubic cell. The structures are viewed along [111], [110], and [100] directions, which correspond to the superlattice. In (a−c), the framework is amorphous, and in (d), the framework is shown after it has crystallized. Sphere model representations of the atom positions; only Mg are shown.

facilitate characterization of the real material. Accordingly, in Figure 11b, a model of ZnO, representative of the real structure (Figure 11a) was generated following the same procedure used to generate models of (FCC) MgO (Figure 10); simulated crystallization of the framework was facilitated by simulating the system under MD at 1500 K. If one inspects the HRTEM, one can observe the close packed channels on the uppermost plane and also see the channels one plane below; careful inspection reveals a third plane of channels, which confirms an "ABC" stacking of the channels. Equipped with both HRTEM and the simulated models, the structure can be further understood and characterized. For example, the surfaces exposed, the single (poly) crystalline nature of the framework, how the framework architecture facilitates ABC (FCC) stacking of "cavities".

The structural stability of these systems is perhaps questionable. Similar to zeolites, they are kinetically driven and thermodynamically less stable compared with the parent (bulk) material—one might also question their mechanical durability. However, there is ample evidence in the literature to show that such framework structures are now being synthesized routinely, with accessible channels and can withstand relatively high temperatures before the architecture collapses to a thermodynamically more stable structure.[23,34] In the following section, we use the simulation strategies to help experimentally rationalize a ZnS superlattice.

ZnS (wurtzite) nanoparticles, with a uniform particle size of 4 nm, were loaded into a diamond anvil cell under low pressure and examined using synchrotron X-ray diffraction at Cornell High Energy Synchrotron Source; X-ray patterns are presented in Figure 12a. The three outer rings reflect the wurtzite crystal structure of ZnS, and the inside spots emanate from the (self-assembled) superlattice comprising the ZnS nanobuilding blocks. The wavelength of the monochromatic beam was 18 keV, using a Mar345 detector with a sample detector separation of 400 mm and a data collection time of 20 min. Analysis of the spots indicates that a mixture of hexagonal and cubic symmetries best fits the data. To further rationalize this data, we generated a structural model. Specifically, spherical ZnS nanobuilding blocks were positioned into a simulation cell with FCC packing and simulated using MD as above; each nanobuilding block is 12 coordinated to its neighbors. The final, low temperature, crystalline structure is shown in Figure 12b−e. The irreducible unit cell, which comprises

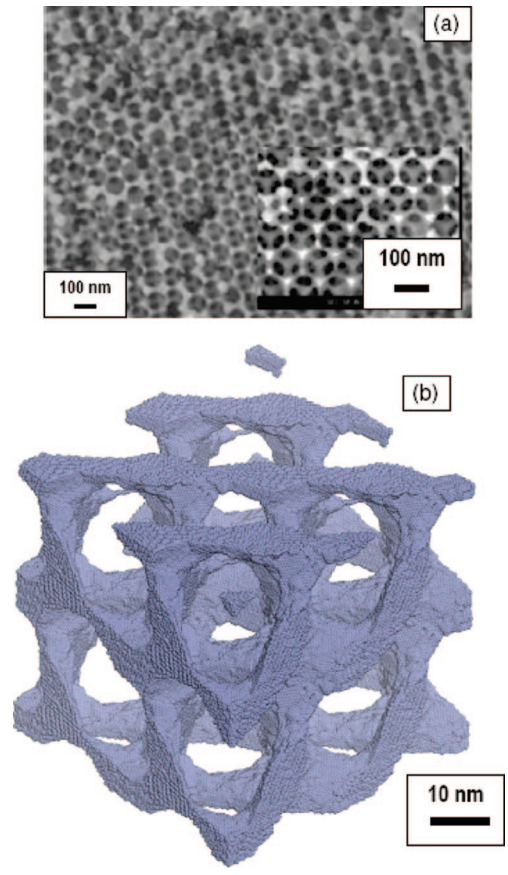

Figure 11. Mesoporous ZnO, experiment and simulation. (a) SEM image, reproduced from ref 33 with permission from Elsevier. (b) Atomistic structure of ZnO generated by positioning ZnO nanobuilding blocks into a cubic cell with FCC packing. The image is viewed along [111] corresponding to the superlattice. Sphere model representation of the atom positions; only the Zn atoms are shown.

100 800 atoms, is shown in Figure 12b. The original (FCC) lattice points of the amorphous ZnS nanobuilding blocks are indicated on the figure by circles, which can help rationalize the structure by revealing how the nanobuilding blocks have agglomerated together into a framework. This unit cell is effectively infinitely repeating (periodic boundary conditions) and a 2 × 2 × 2 cell is shown in Figure 12c, which is annotated to identify {111} planes. In a future study, we will calculate the XRD patterns using models generated by packing nanobuilding blocks together to help rationalize experiment with possible structural models. Slices, cut through the ZnS superlattice, are shown in Figure 12d,e and help explain the complex framework structure. For example, it is clear from the figures that sinusoidal channels (yellow arrow, Figure 12d, traverse the structure.

Hexagonal Crystal Structure/Cubic Superlattice (BCC). In addition to the FCC packing of the ZnS nanobuilding blocks, we also considered BCC packing. The primitive unit cell is shown in Figure 13a, which is annotated with circles to indicate the initial positions and the subsequent agglomeration of the ZnS nanobuilding blocks. In contrast to a coordination number of 12 for an FCC structure, each nanobuilding block has 8 nearest neighbors in a BCC superlattice. However, inspection of the unit cell reveals that one nearest neighbor interaction failed to agglomerate, as indicated by the yellow arrow, and the structure is missing a connecting "arm". A 2 × 2 × 2 supercell is shown in Figure 13b, and a view looking along [111] is shown in Figure 13c. The radial distribution function, calculated for the ZnS nanostructure, is presented in Figure 13d and reveals a broad Zn−S nearest neighbor peak spanning 2.1−2.6 Å with average distance of about 2.3 Å, which is indicative of significant lattice relaxation compared to the bulk parent material.

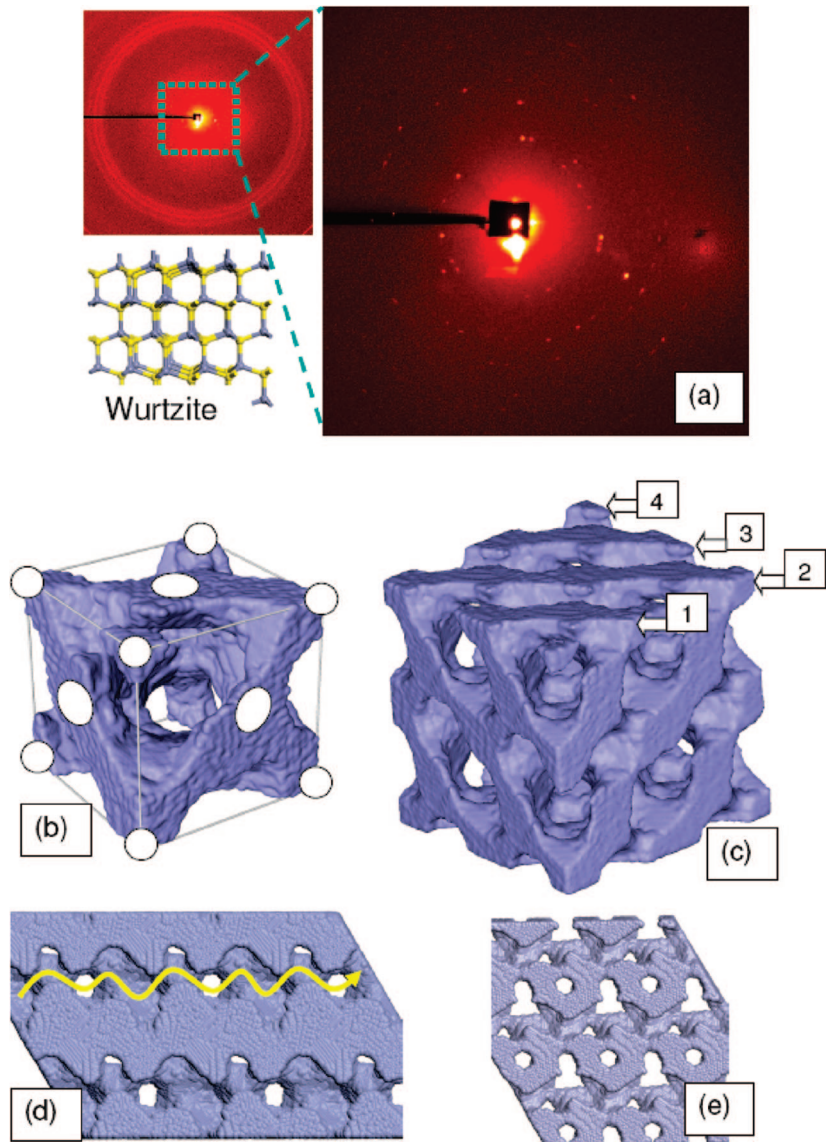

Figure 12. ZnS nanostructure, experiment and simulation. (a) Synchrotron X-ray diffraction patterns of self-assembled ZnS nanoparticles. The three outer rings reflect the wurtzite structure of the nanoparticles and the inside spots emanate from the self-assembled superstructure; (b−e) atomistic models of mesoporous ZnS generated by close packing (FCC) ZnS nanobuilding blocks into a cubic cell; (b) unit cell, the FCC lattice points are indicated by the hollow circles; (c) 2 × 2 × 2 supercell showing more clearly the {111} "planes" corresponding to the superlattice; (d) slice cut through the system revealing a sinusoidal channel that traverses the structure; (e) a slice cut through the system showing more clearly the hexagonal array of channels.

Superlattices from Precrystallized CeO_2 Nanobuilding Blocks. In this section, we use our simulation strategy to help rationalize a ceria nanostructure. In particular, an HRTEM of a ceria superlattice, synthesized by self-assembling (template free) ceria nanocrystals into octahedral superstructures, is presented in Figure 14a. Specifically, individual 3−5 nm ceria nanoparticles, with truncated octahedral morphologies, serve as the building blocks for the octahedral structure (Figure 1). Upon synthesis, these 3−5 nm particles quickly agglomerate to form 15−20 nm superstructures. Further aging allows the particles to reorient into the octahedral morphology through hierarchical structural rearrangement. Wang and Feng found[35] that CeO_2 nanoparticles "agglomerate by minimizing the interface energy with the formation of a lattice matched coherent interface." To generate a fully atomistic model of this structure, we positioned truncated octahedral CeO_2 nanocrystals (generated previously, see ref 8) comprising about 16 000 atoms in a simulation cell with three-dimensional periodic boundary conditions and FCC packing of the nanocrystals; the individual nanocrystals were initially well separated such that, under MD

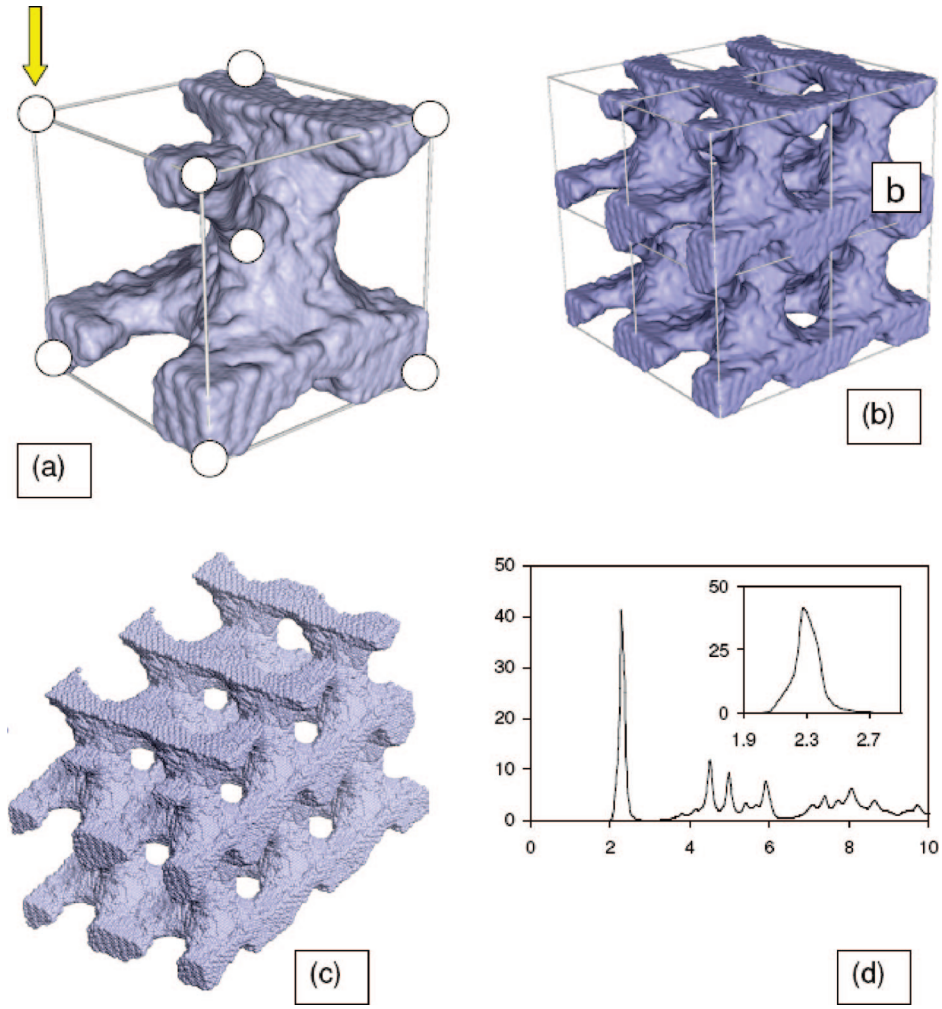

Figure 13. Simulated models of ZnS nanostructure generated by positioning ZnS nanobuilding blocks into a cubic cell with BCC packing: (a) unit cell; BCC lattice positions are indicated by the hollow circles; (b) 2 × 2 × 2 supercell to aid visualization of the porous structure; (c) view looking along [111] with respect to the superlattice. (d) Calculated radial distribution function; abscissa: Zn−S interatomic separation, *r* (angstroms), ordinate: *g*(*r*); (a) and (b) are surface rendered models of the atom positions, and (c) is a sphere model representation of the atom positions; only Zn atoms are shown.

simulation, they could alter their packing. Under constant pressure dynamical simulation, performed at 3400 K, the (strongly attractive) nanocrystals agglomerated into a close packed configuration with alignment of {111}. The model structure (Figure 14b) thus provides insights pertaining to the packing of CeO_2 nanocrystals with truncated octahedral morphologies. We also simulated this nanostructure under high (40 GPa) pressure at 2000 K and found that the system did not anneal into the perfect "bulk" material (within the time scale of the simulation—2000 ps); rather the individual nanobuilding blocks remained intact with the superlattice retaining its hierarchical structure. Experimentally, ceria nanocrystals have been found to resist structural deformation up to 65 GPa.[36]

Thus far we have explored nanostructures generated by assembling nanobuilding blocks of the same materials into superlattices. Clearly an obvious extension to this would be to simulate superlattices comprising two different nanobuilding blocks. Indeed, such binary superlattices, and indeed quasi-ternary superlattices, have recently been synthesized.[37]

Binary Superlattices. Amorphous, spherical (amorphous) MgO and CaO nanoparticles, each comprising 25 200 atoms, were crystallized and placed at FCC positions in a cubic simulation cell (Figure 15a). The system was then compressed (5 GPa) under MD performed at 2000 K for 160 ps, to facilitate compaction of the superlattice (Figure 15b). Inspection of the figure suggests that at this pressure the nanocrystals retain their individual identity. In a second set of MD simulations, a superlattice between MgO and BaO nanobuilding blocks, both comprising 25 200 atoms, was performed as above. Here, the size of the BaO nanobuilding blocks is much larger than the MgO nanobuilding blocks. The simulation cell was filled with the MgO nanoparticles occupying corner positions and BaO nanoparticle at the center (Figure 15c). In Figure 15d, a HRTEM of a binary

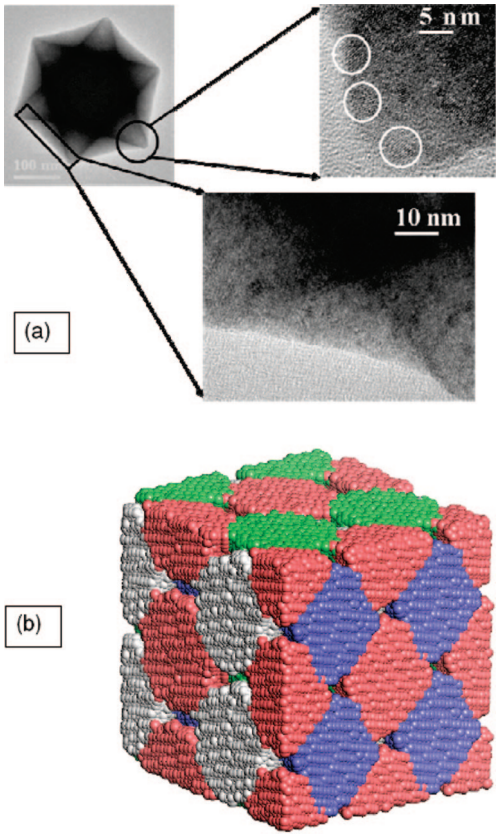

Figure 14. CeO_2 nanoparticle superlattices, experiment and simulated model. (a) Morphological evolution of ceria nanoparticles after 4 weeks of aging in 20% polyethylene glycol (PEG)-based suspensions. The polycrystalline nature of the nanoparticles is evident from the HRTEM images on the right. Individual 3−5 nm ceria nanoparticles (circled) with predominant {111} terminated surfaces self-assemble to achieve the minimum energy configuration. Complete morphological evolution is achieved only after 4 weeks of aging in PEG-based solutions of ceria nanoparticles. (b) Final atomistic structure of CeO_2 nanocrystals that have aggregated, under MD simulation, into a superlattice. The octahedral structure of the nanoparticles facilitates close packing of the individual nanocrystals. The CeO_2 nanocrystals are colored to aid visualization of the individual nanobuilding blocks. Only the Ce ions are shown.

superlattice is shown[20] together with a schematic illustrating the packing of the nanoparticles.

DISCUSSION

From the models generated in this study, we propose that the nanostructure, derived from arrays of nanobuilding blocks, comprises three hierarchical levels of complexity: First, the polymorphic crystal structure of the parent material. Second, microstructural features including, for example, dislocations and grain boundaries. Third, the internal topography or "shape", which comprises the morphology of the cavities and interconnecting channels. Examples of each hierarchical structure are shown in Figure 16. Specifically, Figure 16a shows the 25 200 atom ZnO unit cell "repeat unit", which facilitates a hexagonal array of hexagonal channels. Within this unit cell, we observe using molecular graphics that the ZnO has crystallized into the wurtzite structure. A second polymorph—Isostructural with BCT zeolite[38]—has also evolved in the same unit cell. In Figure 16b, a unit cell of MgO is depicted. Here, the MgO crystallizes into the rocksalt structure. However, to facilitate the porous architecture, the framework is polycrystalline. This observation is supported experimentally by Lu and co-workers, who vacuum crystallized porous (amorphous) MgO to yield a polycrystalline framework architecture.[23]

The results indicate that the crystal structure impacts upon the nanostructure. For example, it is straightforward to imagine channels with square profile being cleaved from MgO, which has a rocksalt (cubic) structure. Similarly, one can envisage channels with hexagonal profiles cleaved from ZnS, which has a wurtzite (hexagonal) structure (Figure 9d). However, when the symmetry of the crystal structure is incommensurate with respect to the symmetry of the superlattice, such as hexagonal channels in (rocksalt) MgO or

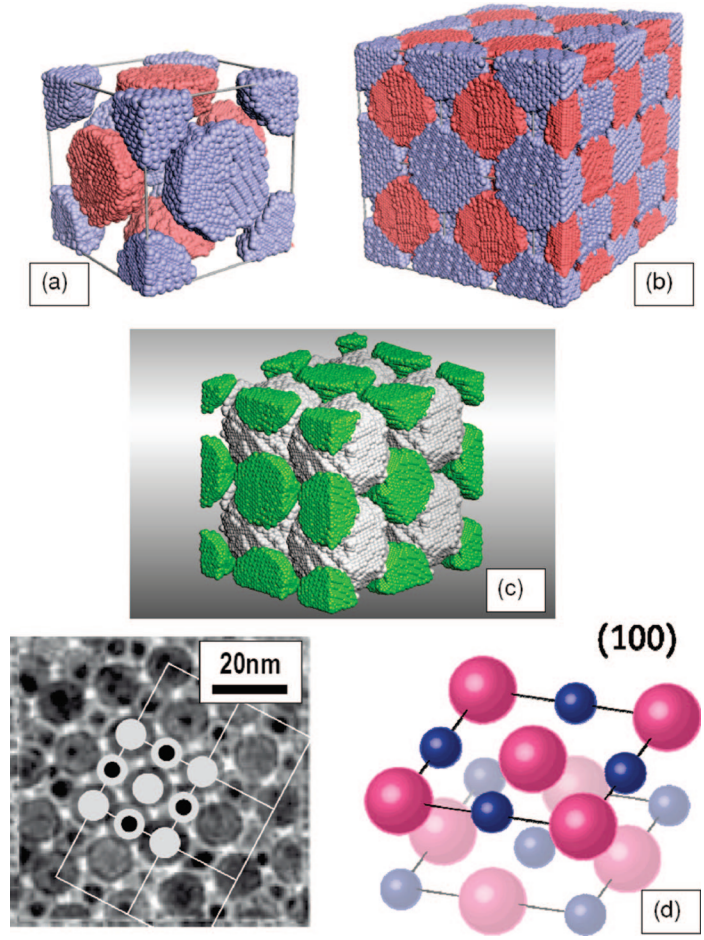

Figure 15. Binary nanoparticle superlattices, experiment and simulated models. (a) Starting structure showing MgO (red) and CaO (blue) nanocrystals at FCC positions in a cubic cell; (b) final structure after MD simulation. The MgO and CaO nanocrystals have aggregated together into a close packed configuration (2 × 2 × 2 supercell shown to aid visualization). (c) Atomistic model of BaO (gray) and MgO (green) conforming to BCC. (d) TEM image of 13.4 nm γ-Fe_2O_3 and 5.0 nm Au with FCC packing of the Fe_2O_3 and Au sublattices (binary superlattice self-assembles into the rocksalt, NaCl structure) adapted with permission from ref 20, copyright 2006 Nature Publishing Group.

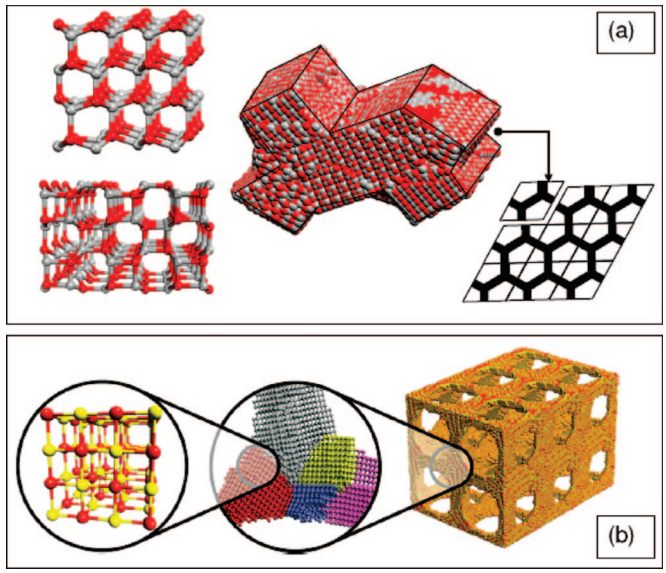

Figure 16. Images depicting three hierarchical levels of structural complexity comprising crystal structure, microstructure, and shape. (a) Shape of ZnO repeat unit facilitating 2D hexagonal array of hexagonal channels. This unit cell comprises two crystal structures. One, top left, conforms to the wurtzite structure, the other, bottom left, is isostructural with BCT zeolite. Zn is colored gray, and oxygen is red; (b) crystal structure (left), microstructure (middle), superlattice structure (right) comprising MgO, which accommodates a 3D array of channels and cavities. Magnesium is colored yellow, and oxygen is red.

a cubic array of channels in (wurtzite) ZnS, then the atomistic structure must respond accordingly. For MgO, we found that hexagonal channels were facilitated by grain boundaries. High curvatures, such as those imposed upon MgO for superlattices comprising FCC arrays of MgO nanoparticles, were facilitated by a complex array of steps and edges (Figure 10d). This structural behavior will change the local strain within the lattice and the coordination numbers of surface ions, which will be reflected in a change in the chemistry associated with the surfaces of the superlattices compared with the parent bulk material. Essentially, there exists a synergistic relationship between the crystal structure, microstructure and nanostructure. Such insights are difficult to measure experimentally,[39] especially deep within the lattice, a region notoriously difficult to probe experimentally,[40] and therefore simulation offers predictive insight into these complex nanostructures.

We note that not all architectures facilitate connectivity between the cavities, such as Figure 14, and therefore flow of gas or liquid through the lattice will not be facilitated by the structure; rather these materials will be important with respect to their mechanical or physical properties.

The surface structure and hence reactivity of the porous materials presented in this study are very different from that presented at the surface of the parent, bulk material. Accordingly, we predict that the chemistry associated with these internal surfaces will also differ. This raises the possibility that one might be able to change or even control the chemistry by facilitating particular architectures.

Reproducibility and statistical significance play important roles in considering these model structures because they are kinetically driven and necessarily metastable. For example, we observed that ZnS nanoparticles, accommodating BCC positions, facilitated a nanostructure where the individual ZnS nanoparticles are coordinated to seven, rather that eight, nearest neighbors. Thus one might perhaps question the reproducibility and hence validity of the results. Upon running similar simulations several times, we did indeed observe slight differences in the final structures, and therefore in the future one must consider statistical sampling of model nanostructures. Indeed, we propose that the real nanomaterial is likely to comprise both seven and eight "coordination numbers"; the relative proportions of each will impact (albeit subtly) upon the properties, and therefore if these models are used to predict properties, then statistical sampling will likely yield more accurate results. We note that each simulation is very expensive computationally (typically seven days using 128 processors), and therefore we do not have much scope for statistical sampling with current computational facilities. However, in a previous study on CeO_2 nanoparticles,[8,28] we found that different starting structures yielded similar final structures, including morphologies, surfaces exposed, surface steps, corners, edges, and other microstructural features such as grain boundaries and dislocations, indicative of reproducible structures.

The statistical nature and reproducibility of the (simulated) crystallization process is perhaps less clear. In particular, during crystallization, a nucleating seed spontaneously evolves. The time required for the seed to evolve appears random, albeit the time can, in part, be influenced by, for example, changing the pressure and temperature and extrinsic doping.[9] If two seeds evolve within the same time scale, then the crystallization front emanating from each seed will impact upon one another, facilitating the evolution of a (general) grain boundary. Such microstructural features are in accord with experiment. Moreover, the materials crystallize into their "correct" crystal structure. Clearly, the simulations are valid in that they accord with experiment, but they also offer a unique insight into the complex statistical nature of crystallization. We also note that the crystallized structures are not influenced artificially; rather the simulator can only change conditions of, for example, temperature, pressure, and solvent.

Experimentally, the statistical nature of synthesis plays a major role in the variety of structures one derives from a particular synthetic pathway. For example, it is very difficult to devise synthetic strategies, which facilitate identical (for example) nanoparticles; rather one observes a variety of nanoparticle shapes, sizes, and morphologies. Sometimes one desires a narrow

structural deviation (tolerance); conversely, one might require a rich variety of different shapes and sizes. In this study, we have simulated the basic synthetic processes that lead to nanostructures. Inevitably this approach, analogous to experiment, leads to issues of reproducibility and statistically driven structural distributions. This is important in a positive way because it means that "simulation" will be in a position to better explain experimental data because it can capture the subtleties pertaining to synthesis and the structures that evolve from such synthetic processes.

CONCLUSIONS

We present a general and systematic simulation strategy for creating models (atom coordinates) of nanomaterials. In particular, we assemble nanoparticles into periodic arrays, using crystallographic rules, and facilitate their aggregation and crystallization into framework architectures. We considered superlattices with cubic, tetragonal, and hexagonal symmetries and primitive (P), FCC, HCP, and BCC packing of the individual nanoparticles; we have also generated models of binary nanoparticle superlattices. The nanomaterials included: CeO_2, Ti-doped CeO_2, ZnO, ZnS, MgO, CaO, SrO, and BaO. The resulting nanomaterials comprise cavities interconnected by channels spanning "zero" (inaccessible cavities), one, two, and three dimensions.

The final fully atomistic models comprised three hierarchical levels of structural complexity: The crystal structure, microstructural features (such as grain boundaries, dislocations, point defects, morphology), and superlattice structure. There is a synergistic interaction between all these hierarchical levels, and therefore if one is to use models to help experiment understand nanostructure and (directly) calculate and thus predict important properties accurately, then one needs to capture all these hierarchical levels in a single model. We have achieved this by simulating the crystallization of each system, starting from amorphous precursors. In particular, it is the *crystallization* (*i.e.*, spontaneous evolution and orientation of nucleating seeds) that facilitates the grain boundaries, dislocations, point defects, internal shape and morphology, and internal surface structure.

A major driving force behind creating metal oxides, with porous crystalline framework architectures, is the promise of "zeolitic chemistry" but spanning a wealth of framework metal ions together with controllable pores and interconnecting channel diameters. Similar to the considerable efforts and insights derived in the field of zeolite simulation,[41,42] the simulations and procedures developed here will prove valuable in helping characterize nanomaterials. In particular, the simulations presented in this study have provided insights pertaining to: The internal morphology of the cavities and interconnecting channels, the (Miller index) surfaces, steps, and edges exposed, which will impact upon the chemistry and reactivity displayed by the internal surfaces. How the curvatures of the channels and cavities are "carved" from the crystallographic structure. The size shape and connectivity of cavities, which will impact upon shape selective catalysis and gaseous/liquid flow including confinement.[43] The influence of microstructural features, such as GB, dislocations, and point defects, which will impact upon transport properties such as ionic transport and electrical conductivity. The (poly-)crystallinity (crystal structure) or amorphicity of the framework walls which will influence the mechanical properties. The strain/lattice curvature within the structure, which will affect the reactivity and physical properties.

We also note that by "simulating synthesis" the resulting structural models are more realistic because they can capture statistically driven structural distributions that inevitably arise as a result of the particular synthetic process. Accordingly, the models derived from the simulations will better explain experimental data and predict important processes or properties.

THEORETICAL METHODS

In this section, we describe the potential models used to represent the interactions between component atoms together with the simulation code and the strategies used for generating the models for the nanomaterials.

Potential Models. All calculations, presented in this study, are based upon the Born model of the ionic solid, in which a charge is assigned to each atom and the long-range attractive interactions between these charged ions are balanced by short-range repulsive (electron−electron) interactions. Model parameters, used to describe CeO_2, Ti−CeO_2, ZnS, ZnO, MgO, CaO, SrO, and BaO, were taken from previous literature.[9,44–46] These potential models have been used extensively previously to model, for example, bulk, surface, and morphological prediction,[9] point and associated defect structures,[47] grain boundaries and dislocations,[48] ionic transport[28] and point defect segregation,[49,50] surface vacancy formation,[49] embryonic crystallization[51] with excellent accord with experiment, and therefore we propose that they will perform reliably for the simulations performed in this present study.

Simulation Code. The DL_POLY code was used to perform all the molecular dynamics (MD) simulations.[52] All simulations were performed using three-dimensional periodic boundary conditions, and therefore the model framework structures represent periodic systems, which are infinitely repeating.

Strategy and Simulation Procedure. Full simulation procedures and conditions including a rationale describing each step can be found in Supporting Information.

Experimental details pertaining to TEM tomography of octahedral CeO_2 nanoparticles can be found in ref 53.

Acknowledgment. We thank J. Churchill for computational support, J. Xiao for providing ZnS samples, S. Kaskel for providing TEM of mesoporous SiO_2 (Figure 5c), and Cambridge-Cranfield HPC facility, EPSRC, AWE, National Science Foundation (CMMI, CBET-NIRT) for funding.

Supporting Information Available: Explicit procedure with guidance notes for generating model framework architectures

via the assembly and crystallization of nanoparticles using MD simulation. This material is available free of charge *via* the Internet at http://pubs.acs.org.

REFERENCES AND NOTES

1. Pileni, M. P. Self-Assembly of Inorganic Nanocrystals: Fabrication and Collective Intrinsic Properties. *Acc. Chem. Res.* **2007**, *40*, 685–693.
2. Niederberger, M.; Colfen, H. Oriented Attachment and Mesocrystals: Non-Classical Crystallization Mechanisms Based on Nanoparticle Assembly. *Phys. Chem. Chem. Phys.* **2006**, *8*, 3271–3287.
3. Urban, J. J.; Talapin, D. V.; Shevchenko, E. V.; Kagan, C. R.; Cherie, R.; Murray, C. B. Synergism in Binary Nanocrystal Superlattices Leads to Enhanced p-type Conductivity in Self-Assembled PbTe/Ag-2 Te Thin Films. *Nat. Mater.* **2007**, *6*, 115–121.
4. Ariga, K.; Hill, J. P.; Ji, Q. M. Layer-by-Layer Assembly as a Versatile Bottom-Up Nanofabrication Technique for Exploratory Research and Realistic Application. *Phys. Chem. Chem. Phys.* **2007**, *9*, 2319–2340.
5. Rodriguez, J. A.; Garcia, M. F. The World of Oxide Nanomaterials. In *Synthesis, Properties and Applications of Oxide Nanomaterials*; Rodriguez, J. A., Garcia, M. F., Eds.; John Wiley & Sons, Inc.: Hoboken, NJ, 2007; pp 1−5.
6. Whitesides, G. M.; Mathias, J. P.; Seto, C. T. Molecular Self-Assembly and NanoChemistry - A Chemical Strategy for the Synthesis of Nanostructures. *Science* **1991**, *254*, 1312–1319.
7. Zhang, H.; Edwards, E. W.; Wang, D. Y.; Mohwald, H. Directing the Self-Assembly of Nanocrystals Beyond Colloidal Crystallization. *Phys. Chem. Chem. Phys.* **2006**, *8*, 3288–3299.
8. Sayle, T. X. T.; Parker, S. C.; Sayle, D. C. Shape of CeO_2 Nanoparticles using Simulated Amorphization and Recrystallization. *Chem. Commun.* **2004**, *21*, 2438–2439.
9. Feng, X. D.; Sayle, D. C.; Wang, Z. L.; Paras, M. S.; Santora, B.; Sutorik, A. C.; Sayle, T. X. T.; Yang, Y.; Ding, Y.; Wang, X. Converting Ceria Polyhedral Nanoparticles into Single-Crystal Nanospheres. *Science* **2006**, *312*, 1504–1508.
10. Glotzer, S. C.; Solomon, M. J. Anisotropy of Building Blocks and Their Assembly into Complex Structures. *Nat. Mater.* **2007**, *6*, 557–562.
11. Smarsly, B.; Antonietti, M. Block Copolymer Assemblies as Templates for the Generation of Mesoporous Inorganic Materials and Crystalline Films. *Eur. J. Inorg. Chem.* **2006**, *6*, 1111–1119.
12. Li, D. L.; Zhou, H. S.; Honma, I. Design and Synthesis of Self-Ordered Mesoporous Nanocomposite Through Controlled *In-Situ* Crystallization. *Nat. Mater.* **2004**, *3*, 65–72.
13. Lei, Y.; Cai, W. P.; Wilde, G. Highly Ordered Nanostructures with Tuneable Size, Shape and Properties: A New Way to Surface Nano-Patterning Using Ultra-Thin Alumina Masks. *Prog. Mater. Sci.* **2007**, *52*, 465–539.
14. Talapin, D. V.; Shevchenko, E. V.; Murray, C. B.; Titov, A. V.; Kral, P. Dipole−Dipole Interactions in Nanoparticle Superlattices. *Nano Lett.* **2007**, *7*, 1213–1219.
15. Majda, D.; Paz, F. A. A.; Friedrichs, O. D.; Foster, M. D.; Simperler, A.; Bell, R. G.; Klinowski, J. Hypothetical Zeolitic Frameworks: In Search of Potential Heterogeneous Catalysts. *J. Phys. Chem. B* **2008**, *112*, 1040–1047.
16. Friedrichs, O. D.; Dress, A. W. M.; Huson, D. H.; Klinowski, J.; Mackay, A. L. Systematic Enumeration of Crystalline Networks. *Nature* **1999**, *400*, 644–647.
17. Marlow, F.; Khalil, A. S. G.; Stempniewicz, M. Circular Mesostructures: Solids with Novel Symmetry Properties. *J. Mater. Chem.* **2007**, *17*, 2168–2182.
18. Glassner, A. Penrose Tiling. *IEEE Comput. Graphics Appl.* **1998**, *18*, 78–86.
19. Chen, D. H.; Li, Z.; Wan, Y.; Tu, X. J.; Shi, Y. F.; Chen, Z. X.; Shen, W.; Yu, C. Z.; Tu, B.; Zhao, D. Y. Anionic Surfactant Induced Mesophase Transformation to Synthesize Highly Ordered Large-Pore Mesoporous Silica Structures. *J. Mater. Chem.* **2006**, *16*, 1511–1519.
20. Shevchenko, E. V.; Talapin, D. V.; Kotov, N. A.; O'Brien, S.; Murray, C. B. Structural Diversity in Binary Nanoparticle Superlattices. *Nature* **2006**, *439*, 55–59.
21. Deshpande, A. S.; Pinna, N.; Smarsly, B.; Antonietti, M.; Niederberger, M. Controlled Assembly of Preformed Ceria Nanocrystals into Highly Ordered 3D Nanostructures. *Small* **2005**, *1*, 313–316.
22. Kuchibhatla, S. V. N. T.; Karakoti, A. S.; Seal, S. Hierarchical Assembly of Inorganic Nanostructured Building Blocks to Octahedral Superstructures - A True Template-Free Self-Assembly. *Nanotechnology* **2007**, *18*, 1–4. (Art. No. 075303)
23. Lu, D.; Katou, T.; Uchida, M.; Kondo, J. N.; Domen, K. *In situ* TEM Observation of Crystallization of Amorphous Ordered Mesoporous Nb-Ta and Mg-Ta Mixed Oxides. *Chem. Mater.* **2005**, *17*, 632–637.
24. Roggenbuck, J.; Tiemann, M. Ordered Mesoporous Magnesium Oxide with High Thermal Stability Synthesized by Exotemplating Using CMK-Carbon. *J. Am. Chem. Soc.* **2005**, *127*, 1096–1097.
25. Roggenbuck, J.; Koch, G.; Tiemann, M. Synthesis of Mesoporous Magnesium Oxide by CMK-3 Carbon Structure Replication. *Chem. Mater.* **2006**, *18*, 4151–4156.
26. Dong, W. Y.; Sun, Y. J.; Lee, C. W.; Hua, W. M.; Lu, X. C.; Shi, Y. F.; Zhang, S. C.; Chen, J. M.; Zhao, D. Y. Controllable and Repeatable Synthesis of Thermally Stable Anatase Nanocrystal-Silica Composites with Highly Ordered Hexagonal Mesostructures. *J. Am. Chem. Soc.* **2007**, *129*, 13894–13904.
27. Sayle, D. C.; Parker, S. C. Encapsulated Oxide Nanoparticles: The Influence of the Microstructure on Associated Impurities Within A Material. *J. Am. Chem. Soc.* **2003**, *125*, 8581–8588.
28. Sayle, T. X. T.; Parker, S. C.; Sayle, D. C. Oxygen Transport in Unreduced, Reduced and Rh(III)-Doped CeO_2 Nanocrystals. *Faraday Discuss.* **2007**, *134*, 377–397.
29. Harding, J. H. The Simulation of General Polar Boundaries. *Surf. Sci.* **1999**, *422*, 87–94.
30. Stankic, S.; Bernardi, J.; Diwald, O.; Knozinger, E. Optical Surface Properties and Morphology of MgO and CaO Nanocrystals. *J. Phys. Chem. B* **2006**, *110*, 13866–13871.
31. Olevsky, E. A.; Tikare, V.; Garino, T. Multi-Scale Study of Sintering: A Review. *J. Am. Ceram. Soc.* **2006**, *89*, 1914–1922.
32. Sayle, D. C.; Feng, X. D.; Ding, Y.; Wang, Z. L.; Sayle, T. X. T. "Simulating Synthesis": Ceria Nanosphere Self-Assembly into Nanorods and Framework Architectures. *J. Am. Chem. Soc.* **2007**, *129*, 7924–7935.
33. Yeo, K. H.; Teh, L. K.; Wong, C. C. Process and Characterization of Macroporous Periodic Nanostructured Zinc Oxide *via* Electrodeposition. *J. Cryst. Growth* **2006**, *287*, 180–184.
34. Deng, Y. H.; Yu, T.; Wan, Y.; Shi, Y. F.; Meng, Y.; Gu, D.; Zhang, L. J.; Huang, Y.; Liu, C.; Wu, X. J. Ordered Mesoporous Silicas and Carbons with Large Accessible Pores Templated From Amphiphilic Diblock Copolymer Poly(ethylene oxide)-b-Polystyrene. *J. Am. Chem. Soc.* **2007**, *129*, 1690–1697.
35. Wang, Z. L.; Feng, X. D. Polyhedral Shapes of CeO_2 Nanoparticles. *J. Phys. Chem. B* **2003**, *107*, 13563–13566.
36. Wang, Z. W.; Seal, S.; Patil, S.; Zha, C. S.; Xue, Q. Anomalous Quasihydrostaticity and Enhanced Structural Stability of 3 nm Nanoceria. *J. Phys. Chem. C* **2007**, *32*, 11756–11759.
37. Shevchenko, E. V.; Kortright, J. B.; Talapin, D. V.; Aloni, S.; Alivisatos, A. P. Quasi-ternary Nanoparticle Superlattices through Nanoparticle Design. *Adv. Mater.* **2007**, *19*, 4183−4188.
38. Hamad, S.; Catlow, C. R. A. Computational Study of the Relative Stabilities of ZnS Clusters, for Sizes Between 1 and 4 nm. *J. Cryst. Growth* **2006**, *294*, 2–8.
39. Wang, Z. L. New Developments in Transmission Electron Microscopy for Nanotechnology. *Adv. Mater.* **2003**, *15*, 1497–1514.
40. Thomas, J. M.; Midgley, P. A. High-Resolution Transmission Electron Microscopy: The Ultimate Nanoanalytical Technique. *Chem. Commun.* **2004**, *11*, 1253–1267.

41. To, J.; Sokol, A. A.; French, S. A.; Catlow, C. R. A.; Sherwood, P.; van Dam, H. J. J. Formation of Heteroatom Active Sites in Zeolites by Hydrolysis and Inversion. *Angew. Chem., Int. Ed.* **2006**, *45*, 1633–1638.
42. Lewis, D. W.; Willock, D. J.; Catlow, C. R. A.; Thomas, J. M.; Hutchings, G. J. *De Novo* Design of Structure-Directing Agents for the Synthesis of Microporous Solids. *Nature* **1996**, *382*, 604–606.
43. Stempniewicz, M.; Khalil, A. S. G.; Rohwerder, M.; Marlow, F. Diffusion in Coiled Pores - Learning from Microrelease and Microsurgery. *J. Am. Chem. Soc.* **2007**, *129*, 10561–10566.
44. Lewis, G. V.; Catlow, C. R. A. Potential Models for Ionic Oxides. *J. Phys. C: Solid State Phys.* **1985**, *18*, 1149–1161.
45. Sayle, D. C.; Mangili, B. C.; Klinowski, J.; Sayle, T. X. T. Simulating Self-Assembly of ZnS Nanoparticles into Mesoporous Materials. *J. Am. Chem. Soc.* **2006**, *128*, 15283–15291.
46. Nyberg, M.; Nygren, M. A.; Pettersson, L. G. M.; Gay, D. H.; Rohl, A. L. Hydrogen Dissociation on Reconstructed ZnO Surfaces. *J. Phys. Chem.* **1996**, *100*, 9054–9063.
47. Khan, M. S.; Islam, M. S.; Bates, D. R. Cation Doping and Oxygen Diffusion in Zirconia: A Combined Atomistic Simulation and Molecular Dynamics Study. *J. Mater. Chem.* **1998**, *8*, 2299–2307.
48. Sayle, D. C.; Catlow, C. R. A.; Dulamita, N.; Healy, M. J. F.; Maicaneanu, S. A.; Slater, B.; Watson, G. W. Modelling Oxide Thin Films. *Mol. Simul.* **2002**, *28*, 683–725.
49. Sayle, T. X. T.; Parker, S. C.; Catlow, C. R. A. The Role of Oxygen Vacancies on Ceria Surfaces in the Oxidation of Carbon-Monoxide. *Surf. Sci.* **1994**, *316*, 329–336.
50. Kenway, P. R.; Oliver, P. M.; Parker, S. C.; Sayle, D. C.; Sayle, T. X. T.; Titiloye, J. O. Computer Simulation of Surface Segregation. *Mol. Simul.* **1992**, *9*, 83–98.
51. Hamad, S.; Cristol, S.; Catlow, C. R. A. Simulation of the Embryonic Stage of ZnS Formation from Aqueous Solution. *J. Am. Chem. Soc.* **2005**, *127*, 2580–2590.
52. Smith, W.; Forester, T. R. *DL_POLY*, copyright by the council for the Central Laboratory of the Research Councils, Daresbury Laboratory, Daresbury, Warrington, UK, 1996; www.cse.clrc.ac.uk/msi/software/DL_POLY/.
53. Xu, X. J.; Saghi, Z.; Gay, R.; Möbus, G. Reconstruction of 3D Morphology of Polyhedral Nanoparticles. *Nanotechnology* **2007**, *18*, 225501.